A Study on the Corrosion Inhibition of Fe-Based Amorphous/Nanocrystalline Coating Synthesized by High-Velocity Oxy-Fuel Spraying in an Extreme Environment

Sapan K. Nayak[1] · Anil Kumar[1] · Kuntal Sarkar[2] · Abhishek Pathak[2] · Atanu Banerjee[2] · Tapas Laha[1]

Abstract In this work, Fe-based (Fe-Cr-B-P-C) amorphous/nanocrystalline composite coatings were deposited by high-velocity oxy-fuel thermal spray method with varying powder feed rates and their behavior in saline environment was investigated. An SS316L coating with optimized parameters was also prepared for comparison purpose. The microstructural characterization of the composite coatings revealed the presence of embedded nanocrystalline phases in the amorphous matrix. The amorphicity of the coating increased, whereas the porosity content decreased gradually with the increment in feed rate during the spraying process. The combined effect of extent of devitrification and porosity content on the corrosion beha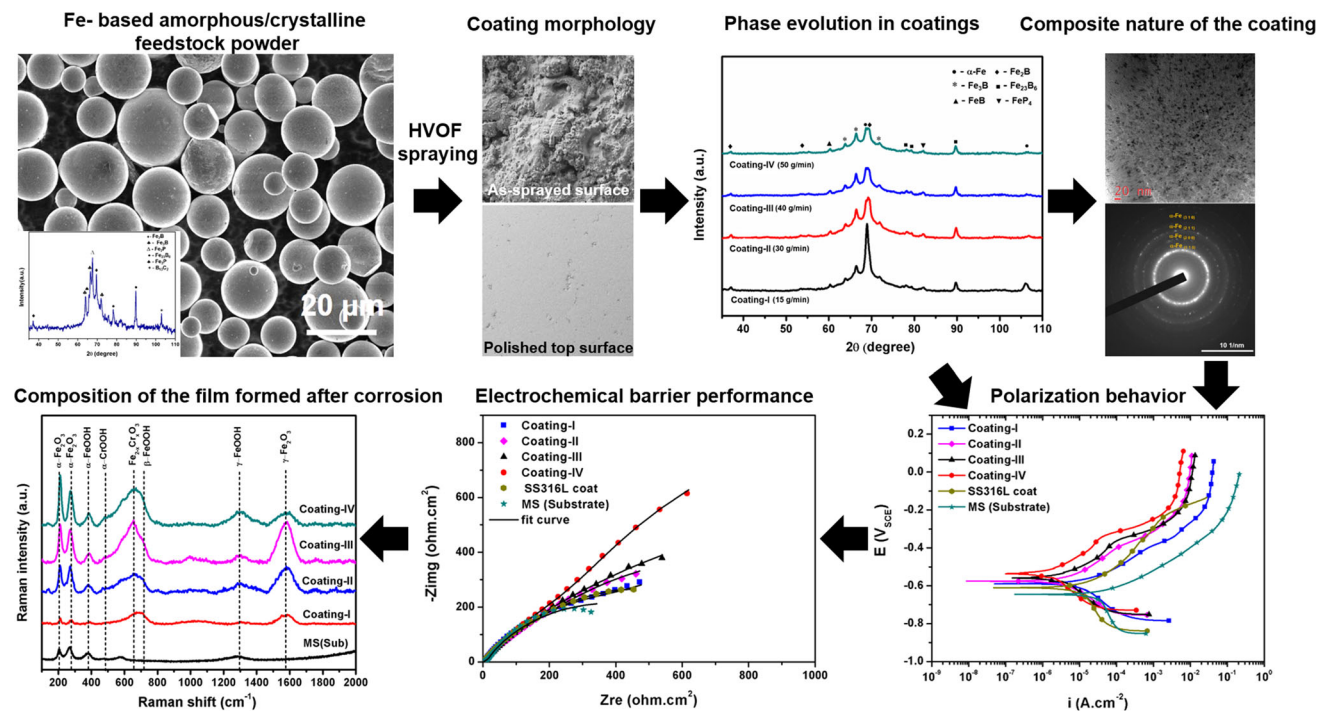vior of the various coatings was analyzed. Potentiodynamic polarization and electrochemical impedance spectroscopy studies revealed that the Fe-based composite coatings exhibited significantly lower corrosion current density and higher polarization resistance than that of the mild steel substrate as well as SS316L coating. The enhanced corrosion resistance of the composite coatings is ascribed to the combined effect of lower porosity content and retained amorphous phase. In addition, the formation of chromium hydroxide along with some of the oxides and hydroxides of iron in the post-corroded coating samples aids in impeding the corrosive solution penetration, thereby increasing the corrosion inhibition efficiency of the composite coatings.

✉ Sapan K. Nayak
sapan.nayak94@gmail.com

Tapas Laha
laha@metal.iitkgp.ac.in

1   Department of Metallurgical and Materials Engineering, Indian Institute of Technology, Kharagpur 721302, India

2   Research and Development Division, Tata Steel, Jamshedpur 831007, India

Graphic Abstract

Fe- based amorphous/crystalline feedstock powder → HVOF spraying → **Coating morphology** (As-sprayed surface / Polished top surface) → **Phase evolution in coatings** → **Composite nature of the coating** → **Polarization behavior** → **Electrochemical barrier performance** → **Composition of the film formed after corrosion**

Keywords corrosion inhibition · EIS · Fe-based amorphous/nanocrystalline composite coating · high-velocity oxy-fuel (HVOF) spraying · polarization · saline environment

Introduction

Bulk metallic glasses (BMGs) exhibit a remarkable combination of mechanical and chemical properties, including superior strength, high hardness and outstanding wear and corrosion resistance attributed to their disordered and defect-free structure, i.e., absence of grain boundaries, slip system, etc. (Ref 1-3). Despite these appealing properties, the industrial application of BMGs is hindered gravely due to their inherent room temperature brittleness and strain softening (Ref 1, 4, 5). Alternately, the preparation of BMG composites with crystalline second phase has proved to be an effective approach to enhance its toughness owing to the hindrance to shear band propagation and promotion of multiple shear band formation caused by the crystalline phase (Ref 6, 7). In addition, limited glass-forming ability (GFA) and inadequate critical casting thickness of monolithic BMGs makes the practical usage of such material very difficult (Ref 8). Accordingly, the synthesis of metallic glass systems as coating on ductile substrate with the thickness in micrometer range can avoid these limitations and widen its

engineering application (Ref 9, 10). The above-mentioned scenarios led to a research drive toward the development of metallic amorphous composite coatings, viz. embedded nanocrystalline precipitates in amorphous matrix. Recently, Fe-based amorphous/nanocrystalline composite coatings prepared via different thermal spraying techniques are being investigated as a surface modification technique for long-term protection of structures in various sectors, including marine environment, oil and gas industries, etc. (Ref 9-12).

Several researchers have explored various thermal spray processes such as arc spray (AS) (Ref 13), atmospheric plasma spray (APS) (Ref 14), kinetic spray (KS) (Ref 15) and high-velocity oxy-fuel (HVOF) spray (Ref 16, 17) to synthesize Fe-based composite coatings owing to the associated higher cooling rate and higher deposition efficiency of the processes. Among the various thermal spray methods, HVOF spraying has been considered extensively as a flexible and versatile and cost-effective technique. The coatings produced by HVOF method possess low porosity and high adhesion strength owing to extremely high velocity encountered by in-flight powder particles (Ref 18, 19). In addition, a fairly high cooling rate in the range of 10^4-10^5 K/s, associated with this process, promotes formation of amorphous structure (Ref 20). However, oxidation of the in-flight particles can incubate the crystallization/devitrification at the inter-splat regions of as-deposited coatings, which largely affects its properties (Ref

32, 33). Zhou et al. (Ref 11) and Zhang et al. (Ref 22) synthesized $Fe_{48}Cr_{15}Mo_{14}C_{15}B_6Y_2$ amorphous coating by HVOF spraying and reported an improvement in corrosion resistance, by optimization of parameters, viz. fuel and oxygen flow. Yang et al. (Ref 21) observed a degradation in the corrosion performance with decreasing fraction of amorphous phases which was attributed to the initiation of corrosion process at the periphery of the crystalline phases. Liu et al. (Ref 23) deposited $Fe_{54.2}Cr_{18.3}Mo_{13.7}Mn_{2.0}W_{6.0}$-$B_{3.3}C_{1.1}Si_{1.4}$ amorphous/nanocrystalline composite coating and noted an improved corrosion resistance in an aggressive hydrochloric acid media. Bakare et al. (Ref 24) synthesized $Fe_{43}Cr_{16}Mo_{16}C_{15}B_{10}$ coating via HVOF spraying and observed that amorphous coating displayed better corrosion inhibition efficiency than its crystalline counterpart. Li et al. (Ref 25) reported a low Cr and Mo-containing Fe-based amorphous alloy; however, the alloy series contained other corrosion-resistant elements like Ni to provide protection.

Thus far, although some studies on the electrochemical corrosion performance of HVOF-sprayed Fe-based amorphous or composite coatings have been conveyed, reported works majorly focused on the Cr-rich and Mo-containing alloying systems which also include high-cost elements like Ni, Cu, Nb, etc. These alloys also contain a large amount of Cr ($\geq$ 15 at.%) and Mo ($\geq$ 14 at.%) which increase the cost, thereby limiting its industrial usage. In addition, the study on Fe-based amorphous coatings with lean compositions of low Cr and without Mo addition is limited to applications in magnetic, electrical fields. This type of Fe-based coatings was not fully explored for the applications involving resistance to corrosion degradation.

From the above-mentioned studies, it can be noticed that the research efforts on the various effects of HVOF parameters on the structural attributes and its subsequent effect on the corrosion resistance of Fe-based composite coating using low Cr and without Mo addition composition are very scant. Accordingly, in the present work, an Fe-based amorphous/nanocrystalline composite coating using a composition having low Cr and without Mo addition was synthesized by HVOF spraying. The principal purpose of this paper stems from addressing the correlation between the combined effect of porosity and amorphicity, resulting from melting through varying the powder feed rate during HVOF process on the corrosion behavior of Fe-based amorphous/nanocrystalline composite coatings in saline environment. In addition, this work aspires to understand the influence of chemical nature and morphology of the corrosion products on the electrochemical behavior of the Fe-based composite coating. Overall, the present work is aimed at systematically investigating the effect of varying HVOF feed rate parameter on the corrosion inhibition efficiency of an inexpensive Fe-based composite coating.

Experimental Procedure

Preparation of the Coatings

The coatings with thickness of about 95 $\pm$ 25 µm studied in this work were prepared from a water-atomized Fe-based amorphous/crystalline feedstock powder (Fe-10Cr-4P-4B-2C, wt.%) deposited onto mild steel substrate of dimension 50 mm $\times$ 20 mm $\times$ 2 mm using a HVOF spraying system (HIPOJET-2700, MEC, India). The substrates were grit blasted and ultrasonically cleaned with ethyl alcohol prior to the spraying process. Oxygen and fuel gas flow rates and spray distance of the HVOF process were kept constant during spraying, whereas the powder feed rate was varied in the range of 15 to 50 g/min to accomplish varying degree of melting and splat solidification. However, the feed rate was not raised above 50 g/min, considering (1) the saturation in the extent of melting and (2) lower bond strength due to reduced heat input of the powder particles at higher feed rate (Ref 26). For comparison purpose, SS316L powder of size in the range of 5-50 µm was also coated on the substrate using industrial parameters. Different HVOF spraying process parameters are depicted in Table 1. The coatings synthesized with varying HVOF process parameters, i.e., increasing powder feed rate, are designated as Coating-I, Coating-II, Coating-III and Coating-IV, respectively.

Characterization of Powder and Coatings

The surface characteristics and morphology of the feedstock powder and coatings were inspected using a scanning electron microscope (SEM, SUPRA 40, Carl Zeiss SMT AG, Germany). Porosity content of the coatings was estimated by area analysis method utilizing ImageJ k 1.45 software on at least ten images (horizontal field width, HFW = 355 µm) of cross-sectional micrographs of the various coatings after polishing. Phase analysis of the feedstock powders and coatings was investigated by x-ray diffraction (XRD, DY1705, Empyrean, PANalytical, Netherlands) in the 2θ range of 35°-110° with a step size of 0.026° using a monochromatic Cr-Kα source. The phase evolution in the coating was further investigated via a transmission electron microscopy (FEG-TEM, JEM-2100F, JEOL). TEM investigation sample was prepared by cutting thin slices of the coated sample of 0.3 mm thick by electrical discharge machining (EDM) and successively thinning down to 30 µm by mechanical polishing using abrasive paper, followed by ion milling with a Gatan

Table 1 Process parameters for Fe-based amorphous/nanocrystalline composite coatings deposited on mild steel substrates by HVOF spraying

Spray parameters	Coatings				
	Coating-I	Coating-II	Coating-III	Coating-IV	SS coat
Oxygen flow rate, SLPM			270		
Fuel gas flow rate, SLPM			55-60		
Air flow rate, SLPM			460		
Carrier gas flow rate, SCFH			15-18		
Spray distance, mm			150		
Powder feed rate, g/min	15	30	40	50	40
Coating thickness, μm			95 ± 25		

precision ion polishing system, model 691, until perforation in the samples.

Electrochemical Corrosion Behavior

The corrosive environment used in the present study is basically aerated 3.5 wt.% NaCl solution. The Cl^- containing solutions are regarded among very aggressive electrolytes which can be ascribed to the deterioration of materials with chloride penetration through the protective surface films. Therefore, the electrochemical corrosion kinetics performance of the coating and mild steel substrate was evaluated using potentiodynamic polarization test with a potentiostat (Interface 1000, Gamry Instruments, USA) at room temperature after 1 h of immersion in the electrolyte, for stabilization of the open-circuit potential (OCP). Prior to starting the corrosion test, the samples were washed in distilled water and ethanol, followed by drying in warm air. A typical flat three-electrode cell, with graphite rod as the counter electrode, a saturated calomel reference electrode (SCE) and coating/substrate as the working electrode, was employed. The polarization test was carried out on a sample of 1-cm^2 exposed area at scan rate of 0.5 mV/s in the potential range of -250 to $+800$ mV, with reference to OCP. Tafel extrapolation method was used to extract the corrosion potentials and corrosion current densities from the polarization curves. EIS analysis was also conducted using the above-mentioned corrosion cell and equipment to explore the stability, viz. barrier performance of the film/s formed on the samples. Impedance values were measured in the frequency range of 100 kHz to 10 mHz, with an applied sinusoidal perturbation of ± 10 mV at OCP. The analysis of the obtained spectra was accomplished using ZView 2.0 software to measure the electrochemical parameters. The surface of the post-corroded samples was characterized by SEM to investigate the morphology of the corrosion products. The corrosion products were also investigated by a Raman spectrometer (InVia Raman Microscope, Renishaw, UK) equipped with a Co laser of 532 nm wavelength.

Results and Discussion

Phase Composition and Morphology of the Feedstock Powder

The morphology, size distribution and phase composition of the feedstock powder are illustrated in Fig. 1. The spherical shape of these particles, shown in Fig. 1(a), corresponds to the characteristic of water-atomized powder (Ref 27). The size distribution chart (Fig. 1b) represents that the size of the particle was varying in the range 5 to 30 μm with a maximum at around 10-20 μm ($d_{50} = 11.2$ μm). The combination of the wider size range and nearly spherical morphology of powders suggest good flowability during the HVOF spraying process. The XRD pattern of the powders is shown in Fig. 1(c), which exhibits a broad protuberance in the 2θ range of 60°-80° with certain amount of crystalline peaks, implying to the amorphous/crystalline nature. The evolution of amorphous phase in the powder is associated with high GFA ($P_{HSS} = -7.31$ kJ/mol) of the Fe-10Cr-4B-4P-2C (wt.%) alloy and reasonably high solidification rate of 10^4-10^6 K/s during water atomization of the powders.

Microstructural Characterization of the Coatings

The morphology of the deposited splats of the various as-received coatings synthesized with different powder feed rates of 15, 30, 40 and 50 g/min is shown in Fig. 2(a)-(e), while the internal porosity structure and their distribution are established from the polished top surface images shown in Fig. 2(f)-(i). Coating-I prepared with the lowest powder feed rate (15 g/min, Table 1), possesses a significantly higher amount of molten particles, which is demonstrated from Fig. 2(a). The extent of molten particles decreased,
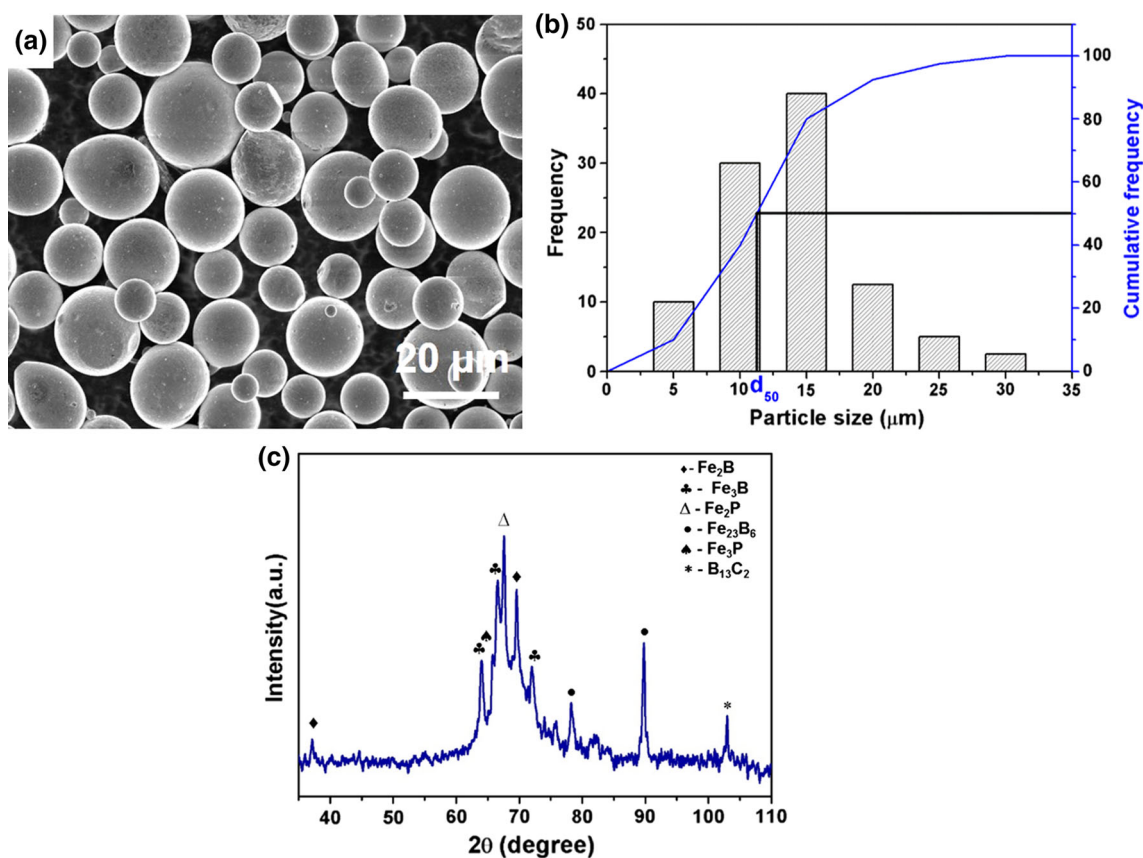
Fig. 1 (a) SEM micrograph, (b) size distribution and (c) XRD pattern of the water-atomized Fe-based (Fe-10Cr-4P-4B-2C, wt.%) amorphous/crystalline feedstock powders used for synthesizing the HVOF-sprayed coatings

and an increment in the partially molten particles was observed, upon increasing the powder feed rate from 15 to 50 g/min gradually (Fig. 2a-d). It was interesting to note that a decreasing trend of porosity content and size was observed when the powder feed rate was increased from 15 to 50 g/min as can be seen from the top polished surface of the coatings (Fig. 2f-i). Additionally, the cross-sectional morphology of the HVOF-sprayed coatings is shown in Fig. 2(j)-(o), which revealed a gradual increment in the inter-splat bonding from Coating-I to Coating-IV. It was also observed that the pore volume fraction decreased with the increment in powder feed rate and the porosity content (vol.%) was 7.1 ± 1.6, 5.6 ± 1.2, 4.7 ± 0.9 and 2.9 ± 0.5 for Coating-I, Coating-II, Coating-III and Coating-IV, respectively. The powder particles during the in-flight process of the HVOF spraying encounter turbulence, which can cause deviation from the trajectory leading to lower deposition rate on the substrate (Ref 28). The maximum amount of porosity at the lowest feed rate is attributed to the lower extent of particle deposition on the substrate due to higher turbulence exerted on the in-flight powder particles with lower feed rate (Fig. 2k). However, the effect of particle deposition frequency gets dissolved gradually with

the increment in powder feed rate resulting in the lowest porosity at 50 g/min powder feed rate (Fig. 2n). Moreover, the decreasing trend in porosity content with the increment in feed rate can be ascribed to (1) filling-up of the pores due to enhanced impingement of particles on the previously deposited splat and (2) amplified shot peening effect of the HVOF method because of the elevated particle bombardment (Ref 29, 30). The SS coating deposited at 40 g/min exhibited greater amount of well-melted particles and porosity content of approximately 2.8 ± 0.4 vol.%, which are shown in Fig. 2(e) and (o).

Phase Evolution of the Coatings

Phase identification of these HVOF-sprayed Fe-based coatings was conducted as shown in Fig. 3. A broad halo peak emerging in the 2θ range of 60°-80° with some crystalline peaks in all coatings inferred the amorphous/nanocrystalline composite nature. Retention of amorphous structure with evolved crystalline phases was observed in all the coatings. The crystalline peaks evolved in the coatings are identified as α-Fe, Fe_2B, $Fe_{23}B_6$, Fe_3B, FeB and FeP_4 phases. The precipitation of crystalline phase
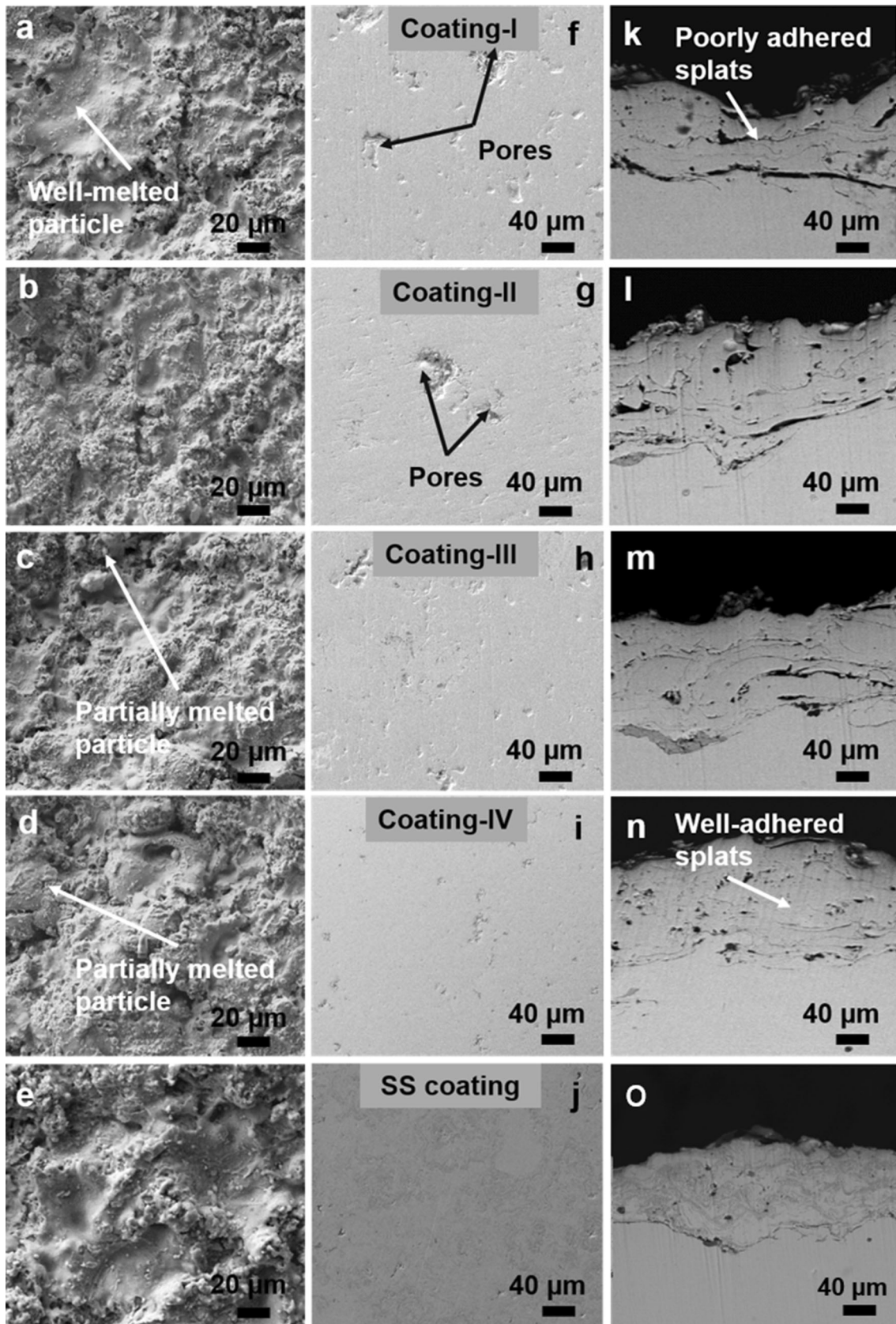
◀**Fig. 2** SEM micrographs of (a-d) as-sprayed, (f-i) polished top surface and (k-n) cross-sectional morphology of the coatings deposited with increasing powder feed rate (15, 30, 40 and 50 g/min), and (e, j and o) SS316L coating, depicting the variation in degree of melting and associated porosity in various coatings

in the amorphous structure can be ascribed to various factors. Higher heat input and greater degree of melting associated with lower feed rate causing a significant amount of crystallization during solidification of splat can be established as one of the factors (Ref [31], [32]). The other factor which can be correlated to the devitrification process is the surface oxidation of the molten powder particles during the spraying process resulting in the nucleation of crystalline phases at the inter-splat boundaries of the synthesized coatings (Ref [20], [21], [33]). The amorphous phase content of the coatings was evaluated using the fraction of integrated areas of the crystalline peaks to the integrated area of the amorphous hump in the XRD spectra (Ref [34]). The amorphous phase fraction was calculated as 72, 80, 83 and 85% for Coating-I, Coating-II, Coating-III and Coating-IV, respectively. These results manifested an increment in amorphous phase content with elevating powder feed rate from 15 to 30 g/min. However, amorphicity of the coatings remained almost the same (80-85%), with further increment in the powder feed rate. The similar range of amorphous content is attributed to the selection of optimized parameters, i.e., oxygen and fuel gas flow rates and spray distance for the feedstock powder used in the present work. Greater extent of melting coupled with high heat input (evident in Fig. 2a) and surface oxidation of powder particles in case of lower feed rate led to higher amount of crystalline phase precipitation in the corresponding coating (Coating-I).
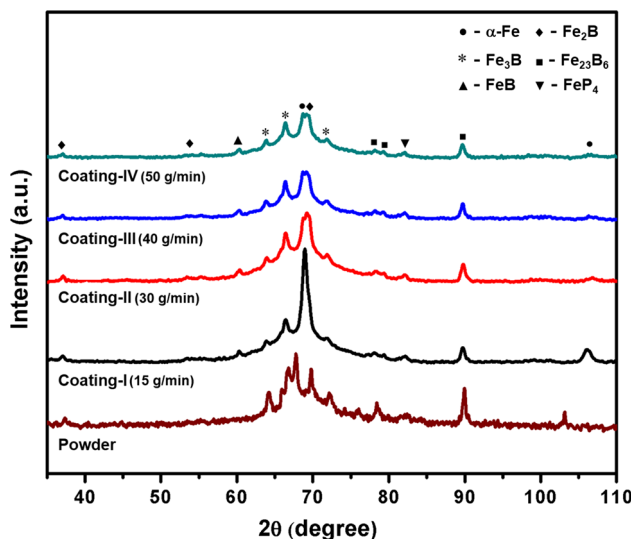
TEM study was undertaken to provide more detailed information regarding the phase evolution in the coatings. As discussed above, there was no significant change in the amorphicity of the coatings with the increment in powder feed rate beyond 30 g/min, establishing Coating-I and Coating-II as the optimal samples for TEM analysis. Figure 4 presents the TEM images along with the corresponding selected area diffraction (SAD) patterns of Coating-I and Coating-II. The TEM micrographs (Fig. 4a and b) illustrated the uniform dispersion of nanocrystalline phases in the amorphous matrix, which is in well accord with the spotty diffused rings observed in the SAD pattern (Fig. 4c and d). The spotty nature of the diffused rings in SAD corresponds to the embedded nanocrystalline precipitates in the amorphous phase, as indicated in Fig. 4(a) and (b). It was observed from the TEM images (Fig. 4a and b) that volume fraction as well as the size of crystalline phases decreased as the powder feed rate increased from 15 to 30 g/min. This result can also be substantiated from the decrease in the number of spots in the diffused SAD patterns of the Coating-II (Fig. 4d) compared to Coating-I (Fig. 4c), which revealed the increase in amorphicity of the coating. The higher devitrification in case of Coating-I can be attributed to the latent heat evolution from the solidified molten splats, associated with the heat input of the molten powder particles during spraying process, leading to localized reheating of the as-deposited coating (Ref [31], [32]). The results obtained from TEM analysis are consistent with the XRD results which confirmed an increase in amorphicity of the coating with the increment in powder feed rate.

Electrochemical Corrosion Behavior

Potentiodynamic Polarization

Typical potentiodynamic polarization plots (E-log i) of the coatings and mild steel substrate in 3.5 wt.% NaCl solution exposed to open air at room temperature are illustrated in Fig. 5. The measured values of corrosion potential (E_{corr}) and corrosion current density (i_{corr}) from various curves are reported in Table 2. As can be seen from Fig. 5(a), the substrate encountered active corrosion over the entire range of anodic polarization scan compared to Fe-based composite coatings, which showed certain amount of passivation without a definite passivating region with low i_{corr} value.

The E_{corr} and i_{corr} of mild steel substrate ($-$ 645 mV and 38.7 μA cm^{-2}) were observed to be more negative and on the higher side, respectively, than that of the coatings indicating the corrosion prone nature of the substrate (Table 2). The composite coatings exhibited higher E_{corr} and lower i_{corr} values, as displayed in Fig. 5(b). The

Fig. 3 XRD patterns of the different coatings deposited with varying powder feed rate displaying variation in crystallization

Fig. 4 TEM images of (a-b) Coating-I and Coating-II with (c-d) corresponding SAD pattern exhibiting the nanocrystalline/amorphous nature of the coating
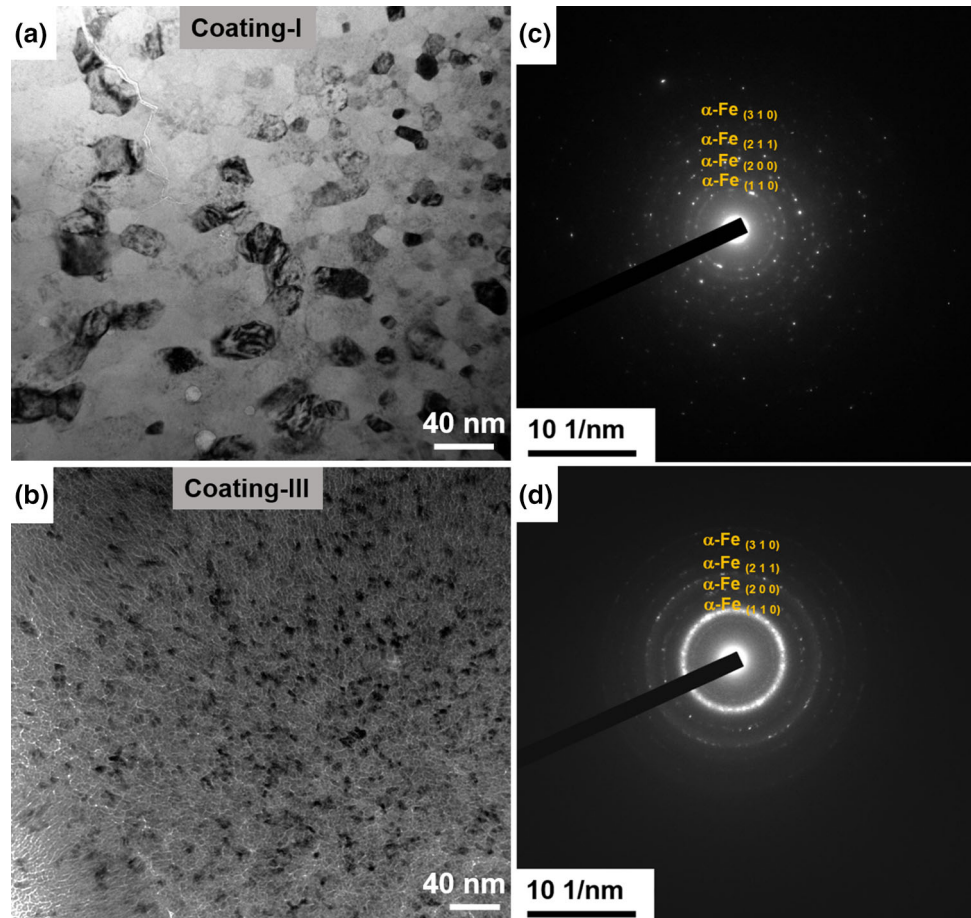
recorded values of E_{corr} and i_{corr} for Coating-I, Coating-II, Coating-III and Coating-IV were $-$ 589 mV, 9.9 μA cm^{-2} (Coating-I), $-$ 576 mV, 5.6 μA cm^{-2} (Coating-II), $-$ 559 mV, 4.4 μA cm^{-2} (Coating-III) and $-$ 536 mV, 2.5 μA cm^{-2} (Coating-IV), reported in Table 2. Moreover, a shifting of corrosion potential toward the nobler side and a decreasing range of corrosion current density was envisaged, upon increasing the powder feed rate gradually from 15 to 50 g/min. On the other hand, the SS coating's E_{corr} ($-$ 610 mV) and i_{corr} (14.3 μA cm^{-2}) was recorded to be in between the substrate and composite coatings.

Evidently, all the composite coatings displayed better corrosion resistance, viz. lower i_{corr} and nobler E_{corr}, than that of the mild steel substrate and also surprisingly than the SS coating having higher chromium content. Although higher amount of chromium in SS coat helped in achieving a less pronounced passivation region, the corrosion tendency was still higher than that of the composite coatings owing to negative E_{corr} and higher i_{corr}. Moreover, the corrosion prone nature of the composite coatings decreased as the feed rate increased from 15 to 50 g/min. The better corrosion resistance of the HVOF-sprayed amorphous/nanocrystalline composite coatings, of same

chemical composition can be assigned to the difference in porosity, i.e., the denseness and the phase evolution resulting from devitrification of amorphous phase.

The existing porosities can lead to degradation of the coating surface attributed to the alteration in passive films through compositional change at the periphery of the pores and creation of occluded regions accelerating the localized corrosion process (Ref 35). Consequently, the presence of porosity can significantly reduce the E_{corr} value, which hastens the corrosion of the coatings. The noblest E_{corr} of the Coating-IV compared to all other coatings, which contain 2.9 $\pm$ 0.5 vol.% porosity (Fig. 2n), is an implication of the restricted micro-galvanic coupling around the interface in the porous regions. The shifting of corrosion potential toward the lower side (more negative) can be attributed to the increment in porosity content (Fig. 2k-n) with the decreased feed rate. Moreover, the crystallinity of the SS coating leads to relatively negative E_{corr} than that of the coatings which can be attributed to the less stable passive film formation its surface.

The above-mentioned electrochemical kinetic parameters (Table 2) illustrate that the corrosion behavior of HVOF-sprayed coatings is significantly affected by the

extent of crystallization. The enhanced corrosion resistance of the Coating-IV (lowest i_{corr} and noblest E_{corr}) was greatly influenced by the higher amorphous phase content (85%). The absence of dislocations, grain boundaries and chemical heterogeneities of the amorphous structure establish the exceptionally high corrosion resistance via formation of homogeneous passive film (Ref 36). It has also been reported that the nanocrystalline precipitates embedded in the amorphous phase can cause preferential

micro-galvanic corrosion initiation at the interparticle interface leading to a degradation in the corrosion resistance of the composite coatings (Ref 21, 33, 37). The lowering of i_{corr} value from 9.9 μA cm^{-2} (Coating-I) to 5.6 μA cm^{-2} (Coating-II) with the increment in feed rate can be accredited to the increased amorphous phase fraction from 72% (Coating-I) to 80% (Coating-II). However, an inconsiderable change in the amorphous content upon elevating the feed rate (> 30 g/min), thereafter, resulted in a similar range of current density (4.4-2.5 μA cm^{-2}). The high i_{corr} value of Coating-I is due to the penetration of solution through the corroded areas around/of the nanocrystalline phases in the coating to interact with the substrate underneath. Besides, the greater degree of melting of the SS coating, shown in Fig. 2(e) and (o), leads to the poor corrosion behavior ($E_{corr} = -$ 610 mV and i_{corr} = 14.3 μA cm^{-2}). The synergistic effect of lower porosity and higher amorphicity results in the best corrosion resistance of Coating-IV ($E_{corr} = -$ 536 mV, i_{corr} = 2.5 μA cm^{-2}).

Electrochemical Impedance Spectroscopy

EIS measurement was taken at OCP on all the coatings as well as substrate in a freely exposed 3.5 wt.% NaCl solution at room temperature to analyze the detailed film formation behavior and the effect of corrosive solution penetration. The results obtained from EIS analysis are consistent with the potentiodynamic polarization results discussed in the previous section. The Nyquist and Bode (phase angle-log v) plots are shown in Fig. 6(a) and (b), respectively. The presence of two consecutive semicircles in the Nyquist plot (Fig. 6a) and two inflection points on corresponding Bode phase plot (Fig. 6b) for all the coatings suggests the associated two time constants except for the substrate, which shows a single time constant. The low-frequency loop could be assigned to the corrosion reaction process, while the high-frequency loop indicates the defectiveness in the coatings (Ref 38, 39).

Considering the above analysis, the electrical equivalent circuits implemented for the simulation of EIS plots illustrated in Fig. 6(c) and (d), respectively. The two circuits comprised of different elements, which are solution
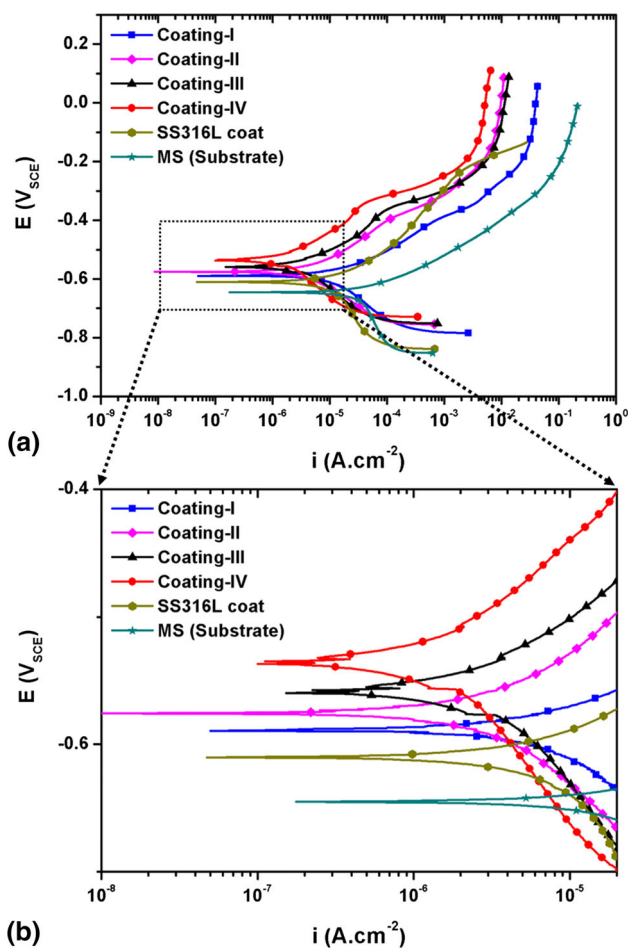

Fig. 5 (a) Potentiodynamic polarization curves obtained from the different coatings and the mild steel substrate, and (b) the corresponding enlarged view of the polarization curves around the OCP values, exposed to 3.5 wt.% NaCl solution

Table 2 Electrochemical kinetic parameters of the various coatings and mild steel substrate estimated from the polarization curves after exposure in aerated 3.5 wt.% NaCl solution

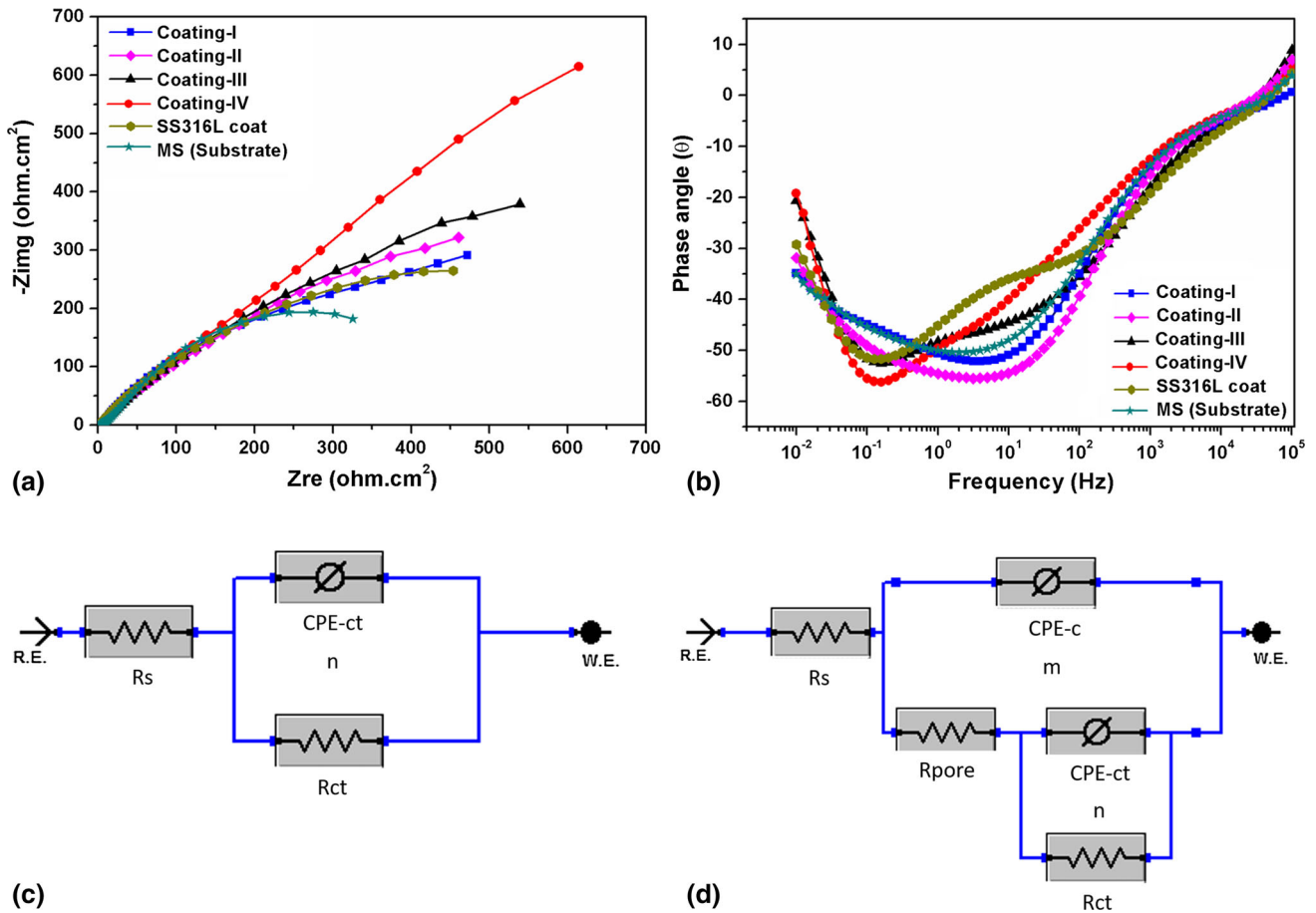| Sample	E_{corr}, mV	i_{corr}, μA cm^{-2}	β_a, mV decade^{-1}	β_c, mV decade^{-1}	CR, mpy
MS (substrate)	− 645 ± 15	38.7 ± 2.5	85	937	17.6
SS coat	− 610 ± 5	14.3 ± 0.7	162	948	6.5
Coating-I	− 589 ± 6	9.9 ± 0.8	91	142	4.5
Coating-II	− 576 ± 3	5.6 ± 0.4	135	158	2.6
Coating-III	− 559 ± 2	4.4 ± 0.4	142	163	2.0
Coating-IV	− 536 ± 3	2.5 ± 0.3	151	196	1.1

Fig. 6 Electrochemical impedance plots of the coatings and mild steel substrate: (a) Nyquist plot, (b) Bode phase angle plot and the electrical equivalent circuits used to fit the impedance data for the (c) mild steel substrate and (d) different coatings

Table 3 Electrochemical impedance parameters of the HVOF-sprayed coatings and mild steel substrate derived from the EIS plots obtained after exposure in 3.5 wt.% NaCl solution at OCP

Sample	R_s, Ω cm²	C_c, μF cm⁻²	m	R_p, Ω cm²	R_{ct}, Ω cm²	C_{ct}, μF cm⁻²	n	R_t, Ω cm²	Goodness of fit, × 10⁻⁴
MS (substrate)	4.3	…	…	…	686	1540	0.61	686	43
SS coat	2.7	4870	0.68	429	930	1063	0.70	1359	3.3
Coating-I	2.1	4960	0.64	438	1010	1131	0.65	1448	4.3
Coating-II	1.8	4710	0.63	529	1160	946	0.78	1689	3.7
Coating-III	2.7	3270	0.61	746	1240	762	0.61	1986	3.5
Coating-IV	2.6	1250	0.66	797	1460	576	0.81	2257	7.1

resistance (R_s) and pore resistance resulting from the hindrance to the ionic conduction paths in the coatings (R_p), the resistance related to the charge transfer phenomena at the coating/substrate interface (R_{ct}), the coating capacitance (C_c) and capacitance associated with the double layer (C_{ct}). The constant phase element (CPE) used in the circuit in place of pure capacitor was due to the inhomogeneous and the porous nature of the coatings. The corrosion

parameters estimated with superior fitting quality with goodness of fit in the range of 10^{-3}-10^{-4} using the equivalent circuits (Fig. 6c and d) are reported in Table 3.

The solution resistance R_s reflects only upon the resistance of the electrolyte used in corrosion test. Thus, a small fluctuation in the R_s value, which is not a material property, is not likely to affect the corrosion process as the value of R_s is very negligible. The pore resistance, R_p, and the

coating capacitance, C_c, signify the extent of the resistance provided by the coating for the electrolyte to diffuse through the layer (Ref 33). It is evident from Table 3 that, with the increment in powder feed rate, the high-frequency loop gradually grows larger (Fig. 6a) implicating the increase in the R_p as well as a decrease in C_c. This is attributed to the better resistance to ionic conduction path to the corrosive solution penetration, as the porosity content decreases from 7.1 ± 1.6 vol.% (Coating-I) to 2.9 ± 0.5 vol.% (Coating-IV) with increasing the feed rate from 15 to 50 g/min. The lower stability of the passive film formed on the SS coating leads to lower R_p (429 Ω cm^2) and higher value of C_c (4870 μF cm^{-2}), shown in Table 3.

The corrosion resistance of the amorphous/nanocrystalline composite coatings would be very much influenced

by the amount of crystallization, leading to a localized attack around/of those regions (Ref 21, 40). The reduction in degree of amorphicity of the composite coatings from 85 (Coating-IV) to 72% (Coating-I), quite evident in Fig. 3, deteriorates the charge transfer resistance, R_{ct}, from 1460 Ω cm^2 (Coating-IV) to 1010 Ω cm^2 (Coating-I). Besides, the decreasing trend of C_{ct} is attributed to the resistance to deterioration of the film formed on the surface of coatings due to the solution penetration through/around the crystalline phases. A lower R_{ct} value (930 Ω cm^2) along with high C_{ct} (1063 μF cm^{-2}) was noticed for the SS coating, owing to the completely crystalline nature of the coating (Fig. 2e).

The extent of corrosion inhibition of the coatings can be predicted by the total resistance, R_t, given by the

Fig. 7 SEM micrographs of the surface of (a-d) the sprayed coatings and (e) SS316L coating, after the potentiodynamic polarization test, illustrating the extent of cracking in the post-polarization samples
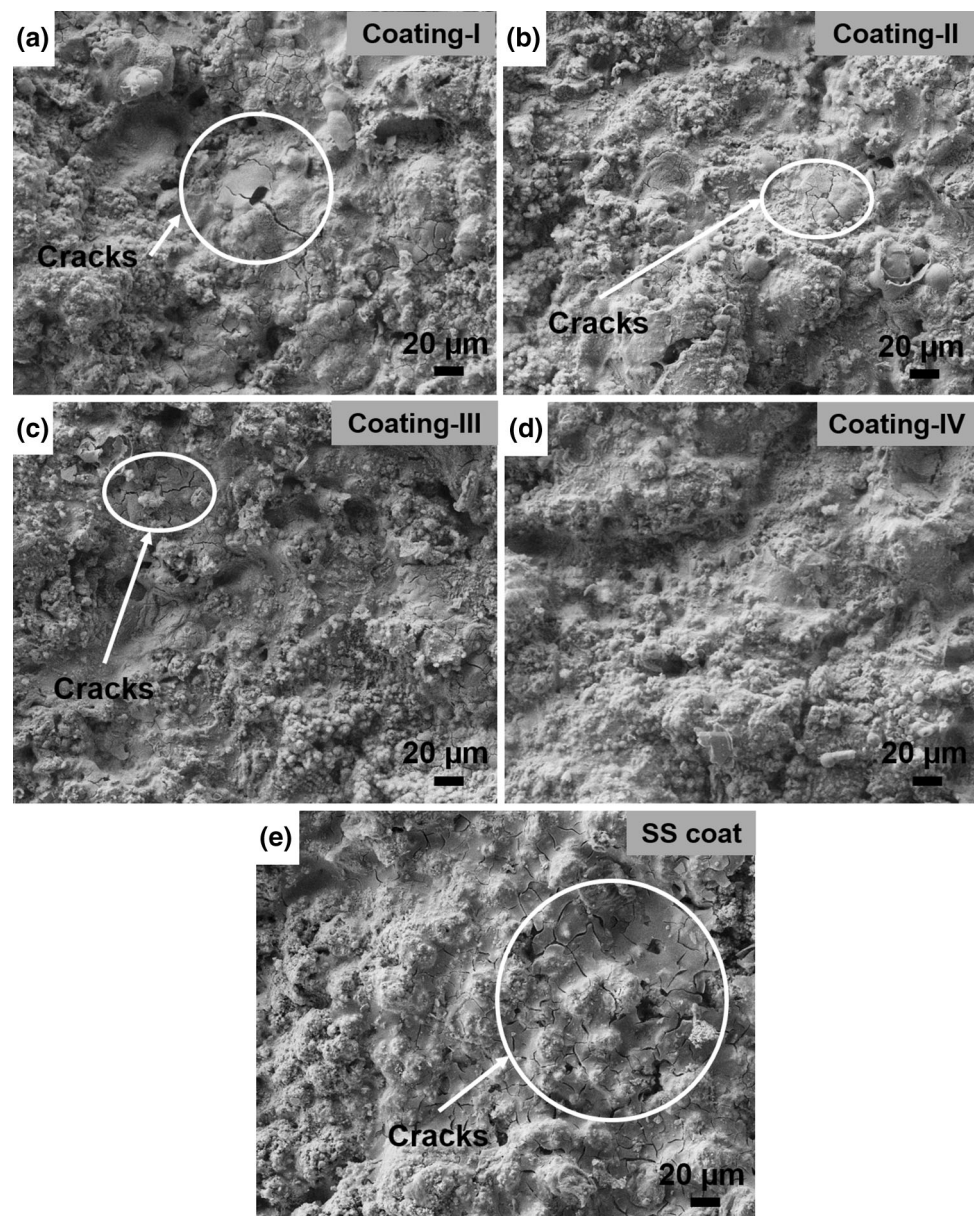
summation of pore resistance (R_p) and the charge transfer resistance (R_{ct}), summarized in Table 3. A highest total resistance of 2257 Ω cm^2 obtained for Coating-IV resulted in the best corrosion inhibition efficiency among all the other coatings in this study. This is consistent with the potentiodynamic polarization results discussed in the previous section (Fig. 5 and Table 2).

Additionally, the behavior of the coatings during corrosion process can also be inferred from the corresponding Bode plot shown in Fig. 6(b). The two inflection points on the Bode plot for the coatings displayed different time constants. The first one lying in the high-frequency range is attributed to the inherent coating property, whereas the second one in the low-frequency region is related to the involved corrosive reactions. The maximum phase angles for Coating-I, Coating-II, Coating-III and Coating-IV were measured as 51°, 55°, 53° and 57°, respectively (Fig. 6b). Although Coating-III displayed a lower phase angle than that of Coating-II, the inflection position at lower-frequency establishes the higher corrosion resistance of Coating-III. Moreover, the phase angle exhibited by Coating-IV (57°) was higher and observed at lower frequency than that of all other coatings indicating better hindrance/barrier behavior toward corrosion process (Ref 40). The lower phase angle of the SS coating (50°) suggests the lower corrosion resistance, which is still higher and at a lower-frequency value than the mild steel substrate (phase angle = 48°). The findings from the Bode plot are in well accord with the discussion of Nyquist plot (Fig. 6a) earlier in this section and polarization results (Fig. 5 and Table 2) in the previous section.

Surface Characterization of the Post-corroded Samples

The corroded surface of all the coatings was investigated further for understanding the corrosion behavior. SEM micrographs of the surface of the various coatings following the corrosion test are shown in Fig. 7. It can be observed from Fig. 7(a)-(d) that extent of cracking in the coatings decreased with the increment in powder feed rate. Almost no cracks were observed for Coating-IV (Fig. 7d) which is the evidence for the highest corrosion inhibition efficiency, i.e., nobler E_{corr}, lowest i_{corr} and highest R_t. The SS coating exhibited larger cracks in a very high amount (Fig. 7e) leading to a lower corrosion resistance. This result matches well with the polarization data (Fig. 5, Table 2) and the EIS analysis (Fig. 6 and Table 3) reported in the earlier sections.

The cracks formed on the corroded surface can be attributed to the various factors leading to ingress of solution through the coating layer, which are (1) the denseness of the coating determined by the porosity

content and (2) the degree of crystallinity in the coating. In addition, the cracking of the corroded surface can be related to the volumetric difference of the corrosion products/rust formed (mainly oxides and hydroxides of the comprising metals) on the coatings.

The further understanding of the corrosion process can be achieved by identifying the corrosion products formed on the surface, for which Raman spectroscopy was employed, and the spectra are illustrated in Fig. 8. The peaks appeared in all the coatings were associated with hematite (α-Fe$_2$O$_3$), akaganeite (β-FeOOH), chromium hydroxide (α-CrOOH), chromium-substituted hematite (Fe$_{2-x}$Cr$_x$O$_3$), goethite (α-FeOOH), lepidocrocite (γ-FeOOH) and maghemite (γ-Fe$_2$O$_3$), except for mild steel (absence of α-CrOOH peak) (Ref 41, 42). The protective nature of α-Fe$_2$O$_3$ and α-FeOOH phases in the rust can be attributed to the stable configuration of Fe and O in the bonding stage. However, a less protective β-FeOOH is expected to form in the salt environment owing to the stabilization of the structure provided by the presence of Cl$^-$ ions (Ref 43). The lepidocrocite (γ-FeOOH) phase is dissolvable phase compared to akaganeite and goethite. However, under the presence of chloride environment, transition of γ-FeOOH to α-FeOOH phase is most likely to occur (Ref 41, 43). Additionally, the stable and compact structure of the Fe$_{2-x}$Cr$_x$O$_3$ establishes a high barrier performance (Ref 42). Besides, phase fraction of the different corrosion products can be correlated with the intensity of their corresponding peaks in the Raman spectra. Therefore, the highest corrosion inhibition efficiency of the Coating-IV can be explained by the existence of α-CrOOH and relatively higher fraction of α-Fe$_2$O$_3$, Fe$_{2-x}$Cr$_x$O$_3$, α-
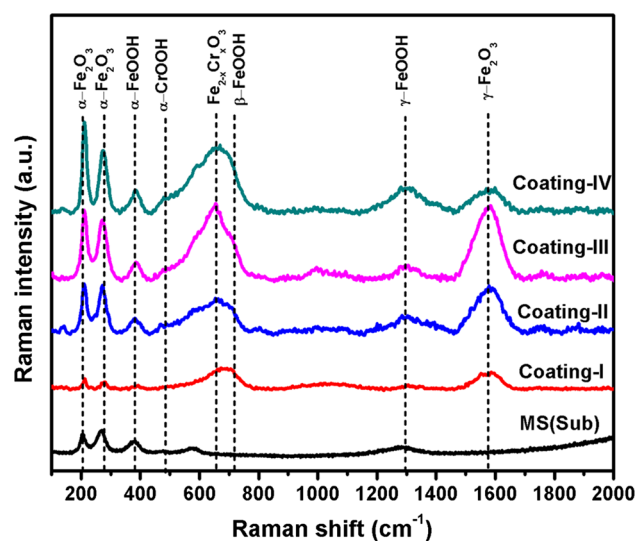

Fig. 8 Raman spectra of the various coatings and the substrate after the potentiodynamic polarization test, depicting presence of chromium hydroxide along with different iron oxides and hydroxides

Fig. 9 SEM images of the (a, c) Coating-I and (b, d) corresponding magnified images after the corrosion test, displaying different morphologies of the products formed, including whiskery shape, clubbed fine crystals and bird's nest-like shape, (e-f) EDS spectrum corresponding to points 1 and 2 of (b)
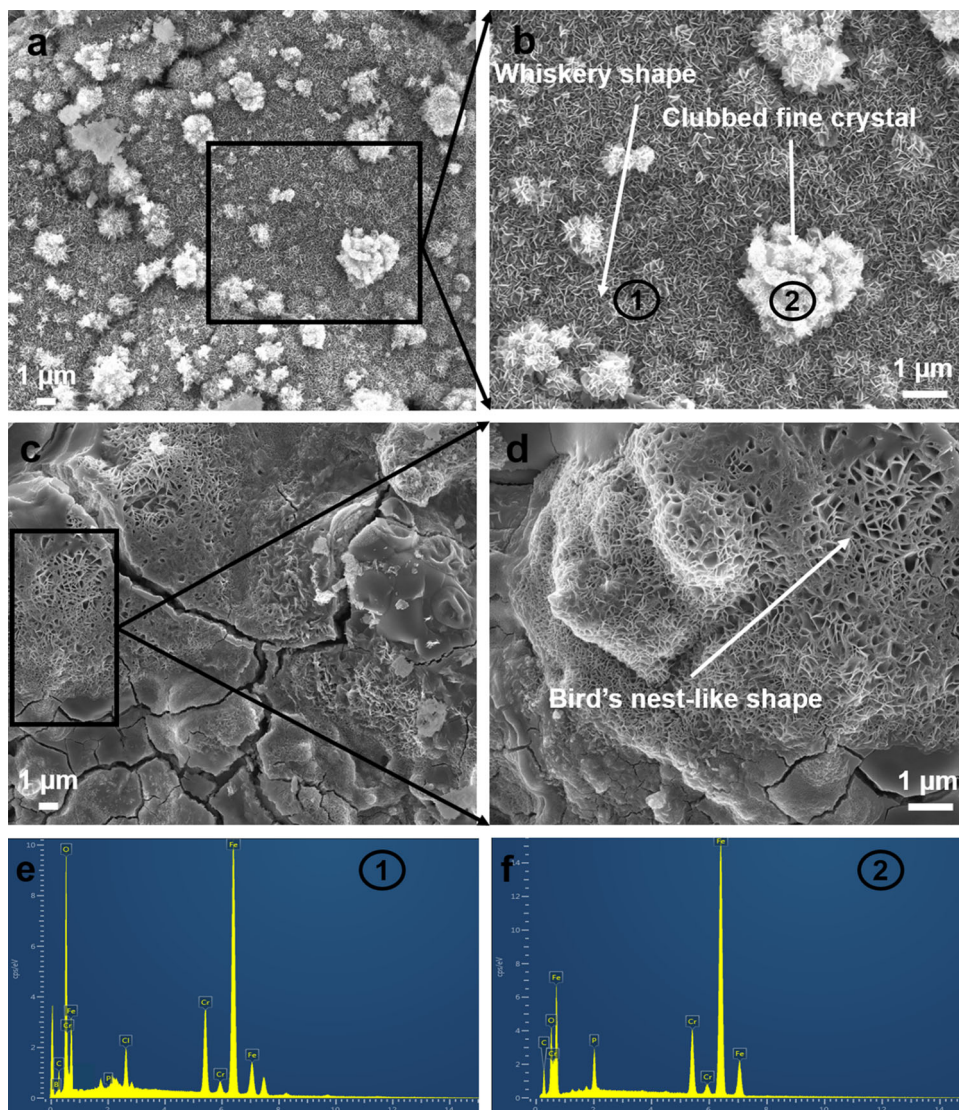
FeOOH and β-FeOOH phases in the film, formed on the surface (Fig. 8).

Moreover, the presence of few of these corrosion products was further confirmed via the SEM micrographs, shown in Fig. 9. The whiskery shape morphology and the clubbed fine crystal structure as shown in Fig. 9(a) and (b) are the characteristic of akaganeite (β-FeOOH) and goethite (α-FeOOH), respectively. However, the bird's nest-like configuration, shown in Fig. 9(c) and (d), is associated with the lepidocrocite (γ-FeOOH) phase (Ref 43). In addition, the EDS analysis of the whiskery area shown in Fig. 9(e) revealed significant amount of chlorine content which confirmed the akaganeite phase. On the contrary, the absence of chlorine in the EDS spectrum of the clubbed fine crystal structure suggested the goethite phase, as shown in Fig. 9(f) (Ref 44).

In summary, the improved corrosion inhibition efficiency of the HVOF-sprayed Fe-based composite coatings can be attributed to the decrement in porosity content and increased amorphicity with the increment in powder feed rate. Moreover, the corrosion resistance for the coatings can also be established by the lessened extent of cracking (Fig. 7), presence of chromium hydroxide phase (evident in Fig. 8) and formation of stable oxides and hydroxides of iron (Fig. 8 and 9). This is consistent with the results analyzed from the polarization curve (Fig. 5 and Table 2) and EIS measurements (Fig. 6 and Table 3), discussed in the above sections.

Conclusions

High corrosion-resistant Fe-based amorphous/nanocrystalline composite coating was deposited on mild steel substrate by high-velocity oxy-fuel (HVOF) spraying using water-atomized amorphous/crystalline feedstock powder

(Fe-10Cr-4B-4P-2C, wt.%) with different powder feed rates. The prominent amorphous nature of the coatings was a result of high glass-forming ability of the alloyed powder and fairly high cooling rate of the HVOF process. The porosity content and the degree of crystallinity (precipitation of nanocrystalline phases) decreased with the increment in feed rate, which were associated with the HVOF shot peening effect and the reduced degree of melting of powder particles, respectively. Coatings deposited with increasing feed rate displayed increased corrosion resistance, depicted from polarization result, i.e., nobler E_{corr} and lower i_{corr}, attributed to their lower porosity and higher amorphous content. Moreover, electrochemical impedance spectroscopy (EIS) measurements illustrated betterment in barrier performance, i.e., higher R_p, R_{ct} and lower C_c, C_{ct} of the film formed on the coating surface with the increment in feed rate. The coating synthesized at highest feed rate of 50 g/min exhibited the best corrosion inhibition efficiency, viz. noblest E_{corr}, lowest i_{corr}, highest R, lowest C_c, highest R_{ct} and lowest C_{ct}, which was attributed to the solution penetration resistance, achieved by lowest porosity content (2.9 ± 0.5 vol.%) and highest amorphicity (85%) of the coating. In addition, no evident cracks and presence of chromium hydroxide phase along with relatively higher fraction of stable oxides and hydroxides of iron on the post-corroded sample enhanced the barrier performance of the coating deposited at highest feed rate. The Fe-based amorphous/nanocrystalline composite coating demonstrated enhanced corrosion inhibition efficiency than that of the mild steel substrate as well as an SS316L coating. The results indicated that the synthesized Fe-based composite coatings have high prospective for the application in marine environment, attributable to the superior corrosion performance.

References

1. C.A. Schuh, T.C. Hufnagel, and U. Ramamurty, Mechanical Behavior of Amorphous Alloys, *Acta Mater.*, 2007, **55**(12), p 4067-4109
2. C. Suryanarayana and A. Inoue, Iron-Based Bulk Metallic Glasses, *Int. Mater. Rev.*, 2012, **58**(3), p 131-166
3. A. Inoue and A. Takeuchi, Recent Development and Applications of Bulk Glassy Alloys, *Int. J. Appl. Glass Sci.*, 2010, **1**(3), p 273-295
4. M.F. Ashby and A.L. Greer, Metallic Glasses as Structural Materials, *Scr. Mater.*, 2006, **54**(3), p 321-326
5. M. Chen, Mechanical Behavior of Metallic Glasses: Microscopic Understanding of Strength and Ductility, *Annu. Rev. Mater. Res.*, 2008, **38**(1), p 445-469
6. S.F. Guo, L. Liu, N. Li, and Y. Li, Fe-Based Bulk Metallic Glass Matrix Composite with Large Plasticity, *Scr. Mater.*, 2010, **62**(6), p 329-332
7. W. Yang, H. Liu, Y. Zhao, A. Inoue, K. Jiang, J. Huo, H. Ling, Q. Li, and B. Shen, Mechanical Properties and Structural Features of Novel Fe-Based Bulk Metallic Glasses with Unprecedented Plasticity, *Sci. Rep.*, 2014, **4**, p 1-6
8. X.J. Gu, S.J. Poon, and G.J. Shiflet, Mechanical Properties of Iron-Based Bulk Metallic Glasses, *J. Mater. Res.*, 2007, **22**(2), p 344-351
9. W. Guo, Y. Wu, J. Zhang, S. Hong, G. Li, G. Ying, J. Guo, and Y. Qin, Fabrication and Characterization of Thermal-Sprayed Fe-Based Amorphous/Nanocrystalline Composite Coatings: An Overview, *J. Therm. Spray Technol.*, 2014, **23**(7), p 1157-1180
10. V. Varadaraajan, R.K. Guduru, and P.S. Mohanty, Synthesis and Microstructural Evolution of Amorphous/Nanocrystalline Steel Coatings by Different Thermal-Spray Processes, *J. Therm. Spray Technol.*, 2013, **22**(4), p 452-462
11. Z. Zhou, L. Wang, F.C. Wang, H.F. Zhang, Y.B. Liu, and S.H. Xu, Formation and Corrosion Behavior of Fe-Based Amorphous Metallic Coatings by HVOF Thermal Spraying, *Surf. Coat. Technol.*, 2009, **204**(5), p 563-570
12. G.Y. Koga, R. Schulz, S. Savoie, A.R.C. Nascimento, Y. Drolet, C. Bolfarini, C.S. Kiminami, and W.J. Botta, Microstructure and Wear Behavior of Fe-Based Amorphous HVOF Coatings Produced from Commercial Precursors, *Surf. Coat. Technol.*, 2017, **309**, p 938-944
13. J.H. Kim and M.H. Lee, A Study on Cavitation Erosion and Corrosion Behavior of Al-, Zn-, Cu-, and Fe-Based Coatings Prepared by Arc Spraying, *J. Therm. Spray Technol.*, 2010, **19**(6), p 1224-1230
14. A. Kumar, R. Kumar, P. Bijalwan, M. Dutta, A. Banerjee, and T. Laha, Fe-Based Amorphous/Nanocrystalline Composite Coating by Plasma Spraying: Effect of Heat Input on Morphology, Phase Evolution and Mechanical Properties, *J. Alloys Compd.*, 2019, **771**, p 827-837
15. J. Kwon, H. Park, I. Lee, and C. Lee, Effect of Gas Flow Rate on Deposition Behavior of Fe-Based Amorphous Alloys in Vacuum Kinetic Spray Process, *Surf. Coat. Technol.*, 2014, **259**, p 585-593
16. B. Movahedi, M.H. Enayati, and C.C. Wong, Structural and Thermal Behavior of Fe-Cr-Mo-P-B-C-Si Amorphous and Nanocrystalline HVOF Coatings, *J. Therm. Spray Technol.*, 2010, **19**(5), p 1093-1099
17. N. Mahata, A. Banerjee, P. Bijalwan, P.K. Rai, S. Sangal, and K. Mondal, Electrochemical Behavior of HVOF-Sprayed Amorphous and Nanocrystalline Fe-Based $Fe_{73.13}Si_{11.12}B_{10.79}Cr_{2.24}$-$C_{2.72}$ Composite Coatings, *J. Mater. Eng. Perform.*, 2017, **26**(11), p 5538-5552
18. M.P. Planche, H. Liao, B. Normand, and C. Coddet, Relationships Between NiCrBSi Particle Characteristics and Corresponding Coating Properties Using Different Thermal Spraying Processes, *Surf. Coat. Technol.*, 2005, **200**(7), p 2465-2473
19. S. Sampath, X.Y. Jiang, J. Matejicek, J. Matejicek, L. Prchlik, A. Kulkarni, and A. Vaidya, Role of Thermal Spray Processing Method on the Microstructure, Residual Stress and Properties of Coatings: An Integrated Study of Ni-5 wt.% Al Bond Coats, *Mater. Sci. Eng., A*, 2004, **364**(1-2), p 216-231
20. H.J. Kim, K.M. Lim, B.G. Seong, and C.G. Park, Amorphous Phase Formation of Zr-Based Alloy Coating by HVOF Spraying Process, *J. Mater. Sci.*, 2001, **36**(1), p 49-54
21. Y. Yang, C. Zhang, Y. Peng, Y. Yu, and L. Liu, Effects of Crystallization on the Corrosion Resistance of Fe-Based Amorphous Coatings, *Corros. Sci.*, 2012, **59**, p 10-19
22. C. Zhang, R.Q. Guo, Y. Yang, Y. Wu, and L. Liu, Influence of the Size of Spraying Powders on the Microstructure and

Corrosion Resistance of Fe-Based Amorphous Coating, *Electrochim. Acta*, 2011, **56**(18), p 6380-6388

23. X.Q. Liu, Y.G. Zheng, X.C. Chang, W.L. Hou, and J.Q. Wang, Influence of HVOF Thermal Spray Process on the Microstructures and Properties of Fe-Based Amorphous/Nano Metallic Coatings, *Mater. Sci. Forum*, 2009, **633-634**, p 685-694

24. M.S. Bakare, K.T. Voisey, K. Chokethawai, and D.G. McCartney, Corrosion Behaviour of Crystalline and Amorphous Forms of the Glass Forming Alloy $Fe_{43}Cr_{16}Mo_{16}C_{15}B_{10}$, *J. Alloys Compd.*, 2012, **527**, p 210-218

25. J. Li, L. Yang, H. Ma, K. Jiang, C. Chang, J.Q. Wang, Z. Song, X. Wang, and R.W. Li, Improved Corrosion Resistance of Novel Fe-Based Amorphous Alloys, *Mater. Des.*, 2016, **95**, p 225-230

26. M. Taheri, Z. Valefi, and K. Zangeneh-Madar, Influence of HVOF Process Parameters on Microstructure and Bond Strength of NiCrAlY Coatings, *Surf. Eng.*, 2012, **28**(4), p 266-272

27. B. Hausnerova, B.N. Mukund, and D. Sanetrnik, Rheological Properties of Gas and Water Atomized 17-4PH Stainless Steel MIM Feedstocks: Effect of Powder Shape and Size, *Powder Technol.*, 2017, **312**, p 152-158

28. M. Li and P.D. Christofides, Modeling and Control of High-Velocity Oxygen-Fuel (HVOF) Thermal Spray: A Tutorial Review, *J. Therm. Spray Technol.*, 2009, **18**(5-6), p 753-768

29. D. Zois, A. Lekatou, M. Vardavoulias, T. Vaimakis, and A.E. Karantzalis, Partially Amorphous Stainless Steel Coatings: Microstructure, Annealing Behavior and Statistical Optimization of Spray Parameters, *Surf. Coat. Technol.*, 2011, **206**(6), p 1469-1483

30. P. Bansal, P.H. Shipway, and S.B. Leen, Residual Stresses in High-Velocity Oxy-Fuel Thermally Sprayed Coatings—Modelling the Effect of Particle Velocity and Temperature during the Spraying Process, *Acta Mater.*, 2007, **55**(15), p 5089-5101

31. L. Qiao, Y. Wu, S. Hong, J. Cheng, and Z. Wei, Influence of the High-Velocity Oxygen-Fuel Spray Parameters on the Porosity and Corrosion Resistance of Iron-Based Amorphous Coatings, *Surf. Coat. Technol.*, 2019, **366**(March), p 296-302

32. Y. Wang, S.L. Jiang, Y.G. Zheng, W. Ke, W.H. Sun, X.C. Chang, W.L. Hou, and J.Q. Wang, Effect of Processing Parameters on the Microstructures and Corrosion Behaviour of High-Velocity Oxy-Fuel (HVOF) Sprayed Fe-Based Amorphous Metallic Coatings, *Mater. Corros.*, 2013, **64**(9), p 801-810

33. J. Wu, S.D. Zhang, W.H. Sun, Y. Gao, and J.Q. Wang, Enhanced Corrosion Resistance in Fe-Based Amorphous Coatings through Eliminating Cr-Depleted Zones, *Corros. Sci.*, 2018, **136**, p 161-173

34. R.S. Maurya, A. Sahu, and T. Laha, Quantitative Phase Analysis in Al86Ni8Y6 Bulk Glassy Alloy Synthesized by Consolidating Mechanically Alloyed Amorphous Powder via Spark Plasma Sintering, *Mater. Des.*, 2016, **93**, p 96-103

35. S.D. Zhang, J. Wu, W.B. Qi, and J.Q. Wang, Effect of Porosity Defects on the Long-Term Corrosion Behaviour of Fe-Based Amorphous Alloy Coated Mild Steel, *Corros. Sci.*, 2016, **110**, p 57-70

36. K. Mondal, B.S. Murty, and U.K. Chatterjee, Electrochemical Behavior of Multicomponent Amorphous and Nanocrystalline Zr-Based Alloys in Different Environments, *Corros. Sci.*, 2006, **48**(8), p 2212-2225

37. C. Zhang, K.C. Chan, Y. Wu, and L. Liu, Pitting Initiation in Fe-Based Amorphous Coatings, *Acta Mater.*, 2012, **60**(10), p 4152-4159

38. K.R. Sriraman, S. Brahimi, J.A. Szpunar, J.H. Osborne, and S. Yue, Characterization of Corrosion Resistance of Electrodeposited Zn-Ni Zn and Cd Coatings, *Electrochim. Acta*, 2013, **105**, p 314-323

39. C. Sun, J. Li, S. Shuang, H. Zeng, and J.L. Luo, Effect of Defect on Corrosion Behavior of Electroless Ni-P Coating in CO_2-Saturated NaCl Solution, *Corros. Sci.*, 2018, **134**, p 23-37

40. J. Wu, S.D. Zhang, W.H. Sun, and J.Q. Wang, Influence of Oxidation Related Structural Defects on Localized Corrosion in HVAF-Sprayed Fe-Based Metallic Coatings, *Surf. Coat. Technol.*, 2018, **335**, p 205-218

41. D. de la Fuente, J. Alcántara, B. Chico, I. Díaz, J.A. Jiménez, and M. Morcillo, Characterisation of Rust Surfaces Formed on Mild Steel Exposed to Marine Atmospheres Using XRD and SEM/Micro-Raman Techniques, *Corros. Sci.*, 2016, **110**, p 253-264

42. K.F. McCarty and D.R. Boehme, A Raman Study of the Systems $Fe_{3-x}Cr_xO_4$ and $Fe_{2-x}Cr_xO_3$, *J. Solid State Chem.*, 1989, **79**(1), p 19-27

43. Y. Ma, Y. Li, and F. Wang, Corrosion of Low Carbon Steel in Atmospheric Environments of Different Chloride Content, *Corros. Sci.*, 2009, **51**(5), p 997-1006

44. A. Mazarío-Fernández, I. Llorente, I. Díaz, A. Gómez-Herrero, M. Morcillo, B. Chico, D. de la Fuente, J.A. Jiménez, J.M. González-Calbet, and J. Alcántara, Environmental Conditions for Akaganeite Formation in Marine Atmosphere Mild Steel Corrosion Products and Its Characterization, *Corrosion*, 2015, **71**(7), p 872-886